Electrical Engineering
https://doi.org/10.1007/s00202-022-01654-w

ORIGINAL PAPER

Bond graph model of line-start permanent-magnet synchronous motors

Amin Mahmoudi[1] · Emad Roshandel[1] · Solmaz Kahourzade[2] · Fardad Vakilipoor[3] · Samuel Drake[1]

Received: 14 May 2022 / Accepted: 12 September 2022

Abstract
The bond-graph (BG) enables to model multi-physics systems in the energy domains. This paper shows that BG models are an alternative, more intuitive and simpler to interpret, graphical tool as compared to existing dynamic models for performance prediction of the line-start permanent-magnet synchronous motors (LSPMSMs). It includes electrical, magnetic, and mechanical energy domains where the stator windings, rotor bars, and permanent magnets are the main components of the model. The dynamical equations of the proposed BG are extracted and solved using the MATLAB ordinary differential equation solver for a sample LSPMSM. The dynamics of the studied LSPMSM is investigated under two operating conditions (1) a healthy motor and (2) a motor with broken rotor bars. The simulation results are compared with the finite-element analysis (FEA) as the most accurate method to simulate the electric motor behaviour. It is shown that the proposed BG model accurately predicts the performance parameters of the motor such as current, torque, and speed under various operating conditions. In addition to the modelling validation, the transient behavior of the LSPMSM are discussed to describe the possible reasons for its behaviour during transient and steady-state operating conditions.

Keywords Bond graph · Dynamics model · Fault analysis · Line-start permanent-magnet synchronous motor · Squirrel cage · Transient analysis

1 Introduction

Electric motors consume more than 50% of the generated electric energy [1]. More than 90% of the electric motors in domestic and industrial applications are line-start squirrel-cage induction motors (SCIMs) [2–4]. The applications of the line-start motors are pumps [5], fans [6], cranes [7], elevators [8], blowers [9], etc. Line-start permanent-magnet synchronous motors (LSPMSMs) have been proposed as a substitute for the SCIMs. Higher efficiency, higher power density, and higher power factor of the LSPMSMs are their main advantageous over the SCIMs [10–13].

Figure 1 compares different types of losses for sample 2.2 kW LSPMSM and SCIM. These motors have the same housing, stator, bearings, and shafts, but different rotor configurations which includes additional four PMs in LSPMSM. Although the rotor rotational losses are ignored in this figure, a similar rotor loss is reasonable for both due to their similar weights (steel density: 7.84 g/cm^3 [14] PM density: 7.7 g/cm^3 [15]). The loss breakdowns (stacked loss bar graphs) illustrate how loss reduction leads to the efficiency improvement. It shows the total losses of the LSPMSM is 40% lower than the SCIM. Since LSPMSMs operate at synchronous speed, the induced eddy current at rotor cage becomes almost zero. Thus, the rotor cage loss nearly vanishes in LSPMS motors except for a negligible harmonic portion. In addition, the ohmic loss of the stator in LSPMS motors, which is the largest portion of the total motor loss, is decreased due to a significant reduction in magnetizing current and thus the input current amplitude of the motors. The less loss of the LSPMSM compared to the conventional IMs enables to have advantages of higher efficiency and power factor as compared to those of IMs [16–18]. In fact, the sample 2.2 kW LSPMSM achieves IE4 efficiency standard while its counterpart SCIM meets IE2 efficiency standard, in a similar volume [19–21].

✉ Emad Roshandel
emad.roshandel@flinders.edu.au

[1] College of Science and Engineering, Flinders University, Adelaide, Australia

[2] STEM, University of South Australia, Adelaide, Australia

[3] Department of Electronics, Information and Bioengineering, Politecnico di Milano, Milan, Lombardy, Italy

Published online: 24 September 2022

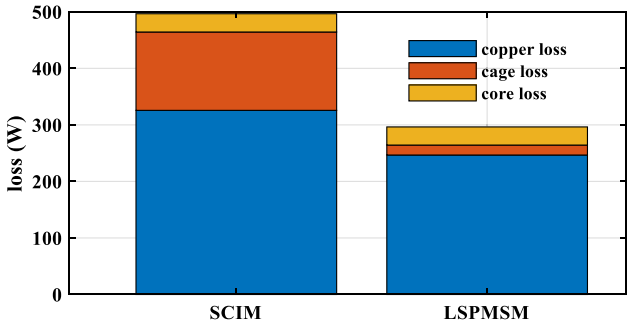

Fig. 1 The comparison of the losses using stacked bar chart for sample 2.2-kW SCIM and LSPMSM extracted from FE simulation. Both studied machines have the same stator, similar rotor outer diameter, but different rotor configurations. The simulation results ignore the rotational losses

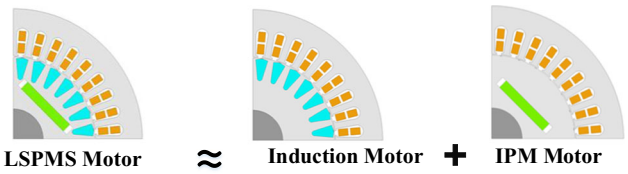

Fig. 2 A visual representation of hybrid rotor line-start permanent-magnet synchronous machine that includes the embedded PMs and a squirrel cage

Figure 2 shows a graphical abstract of the LSPMSM structure. The LSPMSMs stator has three-phase distributed winding like an induction motor. They have a hybrid rotor with embedded permanent magnet (PM) poles and a squirrel cage [22]. The rotor cage adds the line-starting capability to conventional permanent-magnet synchronous motors (PMSMs). So, LSPMSMs start-up like the SCIMs, and their steady-state operation is like the interior PMSMs (IPMSMs).

Often, the electrical motors work as a part of larger electromechanical systems and hence behaviour of the model in association with other components in the systems is vital [23]. The screw compressor [24] and centrifugal pumps [25] are two examples which utilize LSPMSMs in integrated mechanical systems. The dynamic performance prediction of entire system and in real-time control and monitoring necessitate an accurate transient model allows of the system [26]. The BG model allows to easily combine the dynamical equations of a machine with the different devices in a system [27].

The transient finite-element (FE) analysis [4], transient model in *d-q* reference frame (TMRF) [28], and the energy-based models (e.g., Euler–Lagrange equations and bond graph [29, 30]) are techniques for modelling of the transient behavior of electric machines. The well-known transient model in *d-q* reference frame (TMRF) of the electrical motors offer an acceptable accuracy for prediction of the dynamics of LSPMSM [31, 32]. The FE simulations are accurate, but computationally expensive as small-time steps are necessary for transient FE analysis. The FEA also needs the details of the machines like geometry, materials, dimensions, etc. which are not normally available to the users.

Both FE model and TMRF are not a proper approach for prediction of the transient behaviour of the electric motors in the integrated systems. The utilization of FE modelling in an integrated system requires a multi-physics simulation, necessitating a wide range of expertise. Due to the complexity and large computation time, FE analysis may not be suitable for modelling integrated systems. The transient model in *d-q* reference requires inclusion of the electromagnetic equations of the machine to be able to couple them to the other mechanical devices that is not easy.

The bond-graph (BG) is a graphical model in which energy ports are connected by bonds to show the energy transfer between different components of a system. So, they are suitable approach to model an electrical motor in a large electromechanical systems such as jet propulsion engines, turbines, compressors, pumps, and conveyors integrated on the shaft of the motor [33–36]. BG models are useful for process engineers to understand the flow of energy [37, 38].

The ability of the BG models to describe the dynamics of the SCIMs and linear synchronous motors has been studied in the literature [39–42]. However, there is a lack of the LSPMSMs' BG models. This study focuses on the use of bond-graphs and their validity in transient analysis of the LSPMSMs. This paper validates the dynamic performance prediction of a sample line-start motor using BG modelling in both healthy and broken rotor bars conditions. The developed model can be used in the dynamics prediction and condition monitoring applications when LSPMSM are employed in the system. The proposed model can be utilized as a part of a bigger system when the dynamics of an integrated system is the subject of study or analysis like a fully integrated motor/pump System.

In this paper, the stator winding, rotor bars, and permanent magnets of the motor, which play prominent roles in the motor performance, are used to construct the BG model. The accuracy and capability of the proposed model in prediction of the dynamics of LSPMSMs is validated using the finite-element analysis (FEA) results. The findings of this study serve as a platform for future studies involving the dynamics of electromechanical systems in normal or fault conditions. It should be highlighted that the LSPMSM can be connected to a larger system form its input (i.e., electric input voltage) and output (i.e., mechanical load). In this study, the provided BG covers the equations from input to output of the LSMPSMs. The machine performance is examined in no-load and full load tests to illustrate the model capability in prediction of the performance parameters in different loadings. Therefore, the proposed BG can be a proper tool to be used as the equivalent model of the LSPMSMs in an integrated system for

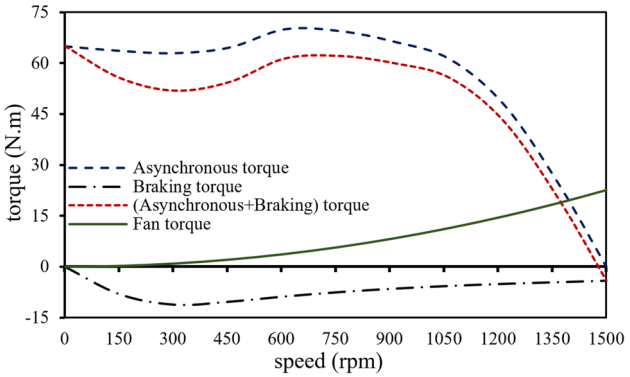

(a) Various torque components in LSPMSMs.

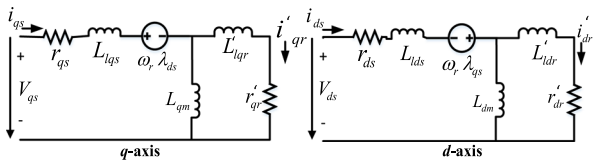

(b) q- and d- axis equivalent circuit of the LSPMSs.

Fig. 3 The breakdown of torque components for line-start permanent-magnet synchronous motor and its electrical equivalent circuit

dynamics analysis in healthy and faulty conditions. The proposed model is fast and accurate which are the characteristics of a suitable model for real-time condition monitoring.

2 Mathematical model

In LSPMSMs, the induction cage located in rotor provides the line-starting capability from the stand-still condition. As shown in Fig. 3(a), the PMs generated torque (braking-torque) reduces the starting torque of the motor compared to a PM free induction motor. The resultant torque of the motor at synchronous speed is summation of the reluctance and PM torques. So, the LSPMSM starts like an IM and operates as an IPMSM in the steady-state condition. To clarify the operating point of a sample fan-load in the torque speed characteristic of the LSPMSM, a fan load torque plotted in Fig. 3a. In fan type load, the torque is proportional to the square of the speed and the resultant torque is formulated as a function of the load torque (T_L) and speed squared (see (1)) [43].

$$T_{\text{fan}} = T_L(1-\text{slip})^2 = T_L\left(\frac{\text{speed}}{\text{Synch peed}}\right)^2, \tag{1}$$

2.1 LSPMSMs dynamics model in d-q reference frame

The dynamics of the motor is studied in the d-q reference frame. Figure 3(b) shows the LSPMSMs electric equivalent circuit (EEC) in d-q frame as presented in [32]. The stator and rotor dynamics equations based on these EECs are written as follow:

$$V_{qs} = r_s i_{qs} + \omega_r \lambda_{ds} + \frac{d\lambda_{qs}}{dt}, \tag{2}$$

$$V_{ds} = r_s i_{ds} - \omega_r \lambda_{qs} + \frac{d\lambda_{ds}}{dt}, \tag{3}$$

$$V'_{qr} = r'_{qr} i'_{qr} + \frac{d\lambda'_{qr}}{dt} = 0, \tag{4}$$

$$V'_{dr} = r'_{dr} i'_{dr} + \frac{d\lambda'_{dr}}{dt} = 0, \tag{5}$$

In the above equations, prime notation ($'$) shows the related rotor parameters referred to the stator side. V_{qs} and V_{ds} are the stator voltages in the d- and q-axis direction. Rotor voltages transferred to the stator side are V'_{qr}, and V'_{dr}; i_{qs}, i_{ds}, i'_{qr}, and i'_{dr} are the stator and rotor currents in the d- and q- axes in stator side; the stator resistance is shown by r_s and rotor resistance referred to the stator side is shown by r'_{qr} and r'_{dr} in the q- and d-axis related equations. Also, the rotor speed and flux linkage are shown by ω_r and λ, respectively. The d-q axes stator side flux linkages for both the stator and rotor are calculated by the following equations.

$$\lambda_{qs} = L_{qs} i_{qs} + L_{qm} i'_{qr} = L_{lqs} i_{qs} + \lambda_{qm}, \tag{6}$$

$$\lambda_{ds} = L_{ds} i_{ds} + L_{dm} i'_{dr} + \lambda_m = L_{lds} i_{ds} + \lambda_{dm}, \tag{7}$$

$$\lambda'_{qr} = L'_{qr} i'_{qr} + L_{qm} i_{qs} = L_{lqr} i'_{qr} + \lambda_{qm}, \tag{8}$$

$$\lambda'_{dr} = L'_{qr} i'_{dr} + L_{dm} i_{ds} + \lambda_m = L_{ldr} i'_{dr} + \lambda_{dm}. \tag{9}$$

The stator and rotor self-inductances transferred to the stator sides are L_{qs}, L_{ds}, L'_{qr}, and L'_{dr}; and the mutual inductances related to the d-q axes are represented by L_{dm} and L_{qm}. In (7) and (9), the permanent magnets flux is shown by λ_m.

2.2 Torque components

The torque of the machine is calculated by (10) when the q-axis flux is independent from the PM flux. The first term is the cage torque (dashed-blue line in Fig. 3(a)), the second term is the reluctance torque, and the third term is the PM torque (dashed-dot line in Fig. 3(a)). The second and third terms produce the synchronization torque. The interaction of these terms results in a success or failure in starting and hence synchronization.

The starting and synchronizing of line-start PM motors are challenging issues, primarily due to the braking torque of the magnet poles. This braking torque is zero at starting and reaches a maximum value at low speed before falling as the speed increases. This braking torque can cause vibration and noise during the starting period of the line-start PM motors.

2.3 Matrix form of the LSPMSMs dynamics model

The resistances and inductances of an electric machine are the energy variables of the system which are required in a BG model. In this section, the LSPMSMs dynamics model is formulated based on the energy variables in a matrix form to facilitate the implementation of BG modelling. The first step is to find the relationship of the motor inductances to the voltage and current. So, the calculated flux linkages in (6) to (9) are substituted with their value in (2) to (5). The matrix form of the LSPMSM dynamic model is obtained by this substitution shown in (11).

The matrix form of the flux relationship with the currents are needed to find the energy conversion relationship between the stator and rotor. These matrices, presented in (12), are obtained based on (6) to (9).

$$\underbrace{T_{em} = (3p/2)\left(\lambda_{ds} i_{qs} - \lambda_{qs} i_{ds}\right)}_{Total\ torque}$$
$$= \underbrace{(3p/2)\left(L_{ds} - L_{qs}\right) i_{qs} i_{ds}}_{cage\ torque} \underbrace{(3p/2)\left(L_{dm} i_{dr}^{'} i_{qs} - L_{qm} i_{qr}^{'} i_{ds}\right)}_{reluctance\ torque}$$
$$+ \underbrace{(3p/2)\,\lambda_m i_{qs}}_{PM\ torque} \tag{10}$$

$$\begin{bmatrix} V_{qs} \\ V_{ds} \\ 0 \\ 0 \end{bmatrix} = \begin{bmatrix} R_s + L_{qs}\frac{d}{dt} & \omega_r L_{ds} & L_{qm}\frac{d}{dt} & \omega_r L_{dm} \\ -\omega_r L_{qs} & R_s + L_{ds}\frac{d}{dt} & -\omega_r L_{qm} & L_{dm}\frac{d}{dt} \\ L_{qm}\frac{d}{dt} & 0 & r_{qr}^{'} + L_{lqr}\frac{d}{dt} & 0 \\ 0 & L_{dm}\frac{d}{dt} & 0 & r_{qr}^{'} + L_{ldr}\frac{d}{dt} \end{bmatrix} \begin{bmatrix} i_{qs} \\ i_{ds} \\ i_{qr}^{'} \\ i_{dr}^{'} \end{bmatrix} + \begin{bmatrix} \omega_r \lambda_m \\ 0 \\ 0 \\ 0 \end{bmatrix} \tag{11}$$

$$\begin{bmatrix} \lambda_{qs} \\ \lambda_{qr} \end{bmatrix} = \begin{bmatrix} L_{qs} & L_{qm} \\ L_{qm} & L_{qr}^{'} \end{bmatrix} \begin{bmatrix} i_{qs} \\ i_{qr}^{'} \end{bmatrix}, \tag{12a}$$

$$\begin{bmatrix} \lambda_{ds} \\ \lambda_{dr} \end{bmatrix} = \begin{bmatrix} L_{ds} & L_{dm} \\ L_{dm} & L_{dr}^{'} \end{bmatrix} \begin{bmatrix} i_{ds} \\ i_{dr}^{'} \end{bmatrix} + \begin{bmatrix} \lambda_m \\ \lambda_m \end{bmatrix}. \tag{12b}$$

The motor torque dynamics considering the inertia (J) and the damping factor (c) is as follows:

$$T_{em} = J\frac{d\omega_m}{dt} + c\omega_m + T_L, \tag{13}$$

where T_L and ω_m are the load torque and speed of the motor, respectively. So, the relationship of the developed electromagnetic torque with the load torque, inertia, and damping factor is written in (14) to be investigated in the preparation of the BG model.

$$(3p/2)\left(\lambda_{ds} i_{qs} - \lambda_{qs} i_{ds}\right) = J\frac{d\omega_m}{dt} + c\omega_m + T_L. \tag{14}$$

The presented electric circuit matrix in (11), the flux relationship with current shown in (12), and the torque balance equation written in (14) are used to find the BG model of the LSPMSM.

3 Bond graph model

The BG model is prepared in two different stages. First, a direct bond-graph model which is obtained based on the d-q reference model of the LSPMSM. Second, the developed direct bond-graph is extended to achieve a separated current for each rotor bar and it is named BG model.

In BG, the voltage and torque are called "efforts" whereas the current and rotational speed are "flows". A simple transformer shown by (TF) determines the relationship of effort to effort and flow to flow. The gyrators (GYs) are used when a flow at one side applies an effort to another side and vice-versa. The modulated gyrators (MGYs) are employed when the coupling between variables depends on external variables.

3.1 Simple bond-graph

Considering the obtained dynamics equations, the BG model of the LSPMSM is developed. In the first step, the three-phase voltages are transferred to the d-q axes reference frame using the Park transform. The required modulated transfer functions (MTFs) of the three-phase to two phases, shown by ms1 to ms6 in Fig. 4, are tabulated in Table 1.

The electrical energy of the energy sources is dissipated into the winding resistors and converted to the magnetic and mechanical energies. According to the flux linkage matrix shown in (12), four modulated gyrators (MGYs) are required to find the magnetic energy produced by the applied electrical energy. There is a magnetic term (λ_m) in (14b) which appears as a gyrator (GY) in the BG model. The MGYs and GY are tabulated in Table 1.

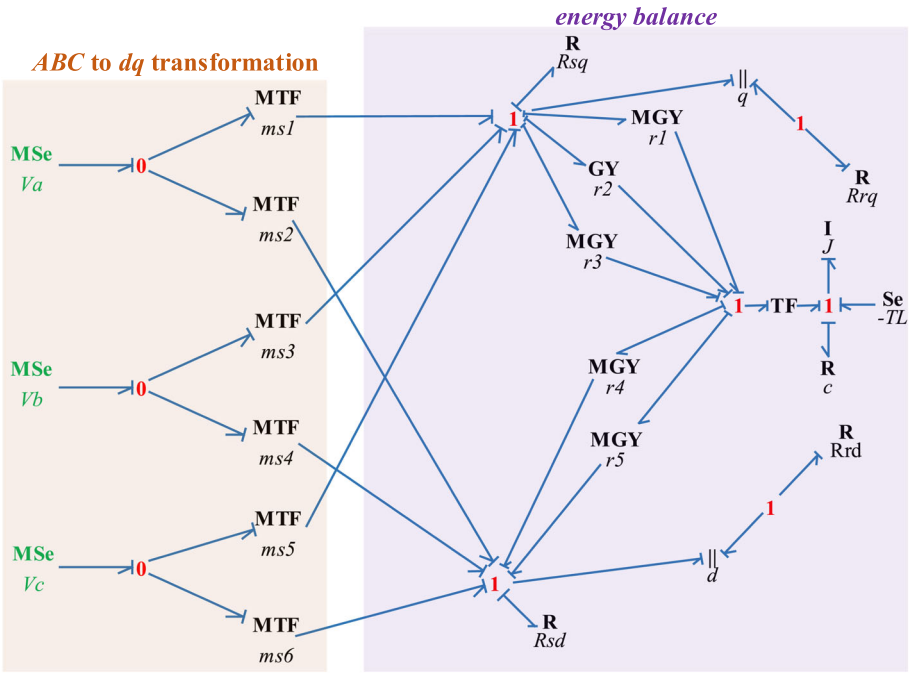

Fig. 4 The proposed general bond-graph of the LSPMSM based on the *d-q* axes EEC. MSe: modulated electrical source; MTF: modulated transformer; MGY: modulated gyrator; GY: gyrator; R: resistance; Se: mechanical load; J: inertia; TF: transformer. ms1 to ms5 are the transfer functions defined in Table 1. r1 to r5 are the gyrators and modulated gyrators defined in Table 1

Table 1 The transformation in the proposed BG model of the LSPMSMs

Transformation	Equation	
MTF: ms1	$\frac{2}{3}\cos(\theta_r)$	(15)
MTF: ms2	$\frac{2}{3}\sin(\theta_r)$	(16)
MTF: ms3	$\frac{2}{3}\cos(\theta_r - \frac{2\pi}{3})$	(17)
MTF: ms4	$\frac{2}{3}\sin(\theta_r - \frac{2\pi}{3})$	(18)
MTF: ms5	$\frac{2}{3}\cos(\theta_r + \frac{2\pi}{3})$	(19)
MTF: ms6	$\frac{2}{3}\sin(\theta_r + \frac{2\pi}{3})$	(20)
MGY: r1	$L_{ds}i_{ds}$	(21)
GY: r2	λ_m	(22)
MGY: r3	$L_{dm}i'_{dr}$	(23)
MGY: r4	$L_{qs}i_{qs}$	(24)
MGY: r5	$L_{qm}i'_{qr}$	(25)

The rotor bar's resistance is another source of the dissipation of energy which is considered in the model. According to (11), which shows the voltage balance of the LSPMSMs, the *d-q* axes rotor resistances have a linear relationship with the rotor side voltage and is mapped in the BG model. The simple BG model of the LSPMSM which works for a motor with the healthy rotor bars is presented in Fig. 4. This model uses the proven concept in [41] that the stator and rotor resistances of a three-phase model are equal to their equivalent resistances in the *d-q* references frame. In Fig. 4, the stator resistance (winding resistance of each phase) is shown by R_{sq} and R_{sd}. The rotor resistance which is equal to the equivalent rotor cage resistance is shown by R_{rq} and R_{rd} for *d-q* voltage equations.

3.2 Consideration of the separated rotor bars in BG model

One of the benefits of using the BG model is the detailed consideration of the system. The proposed BG model in previous section lacks the investigation of each rotor bar separately. So, its application is limited to the study of a LSPMSM when it operates in a healthy condition.

In this section, the rotor resistance branch of the BG model shown in Fig. 4 is extended to improve the capability of the BG model in prediction of the LSPMSMs in faulty condition. In the updated model, the stator resistance in both *d*- and *q*-axis is shown by R_{sq} and R_{sd} which are equal to the stator phase winding resistances. However, the rotor resistance is considered for each single rotor bar. These values are shown by R_{r1} to R_{r5} for a sample five bats machine.

The rotor bars have a similar dimension and are placed in parallel to each other. So, their currents are equal. Like the proposed model for calculation of the current in the IM cage, the rotor bar currents are calculated by (26) [44].

$$i_{rk} = m\left[i_{rq}\cos\left(\theta + \frac{2(k-1)\pi}{n}\right) + i_{rd}\sin(\theta + \frac{2(k-1)\pi}{n})\right], \tag{26}$$

where n and m are the number of rotor bars and modulation index, respectively; and θ is the rotor bar angle in electrical degrees. Considering (26), the relationship of the rotor bars

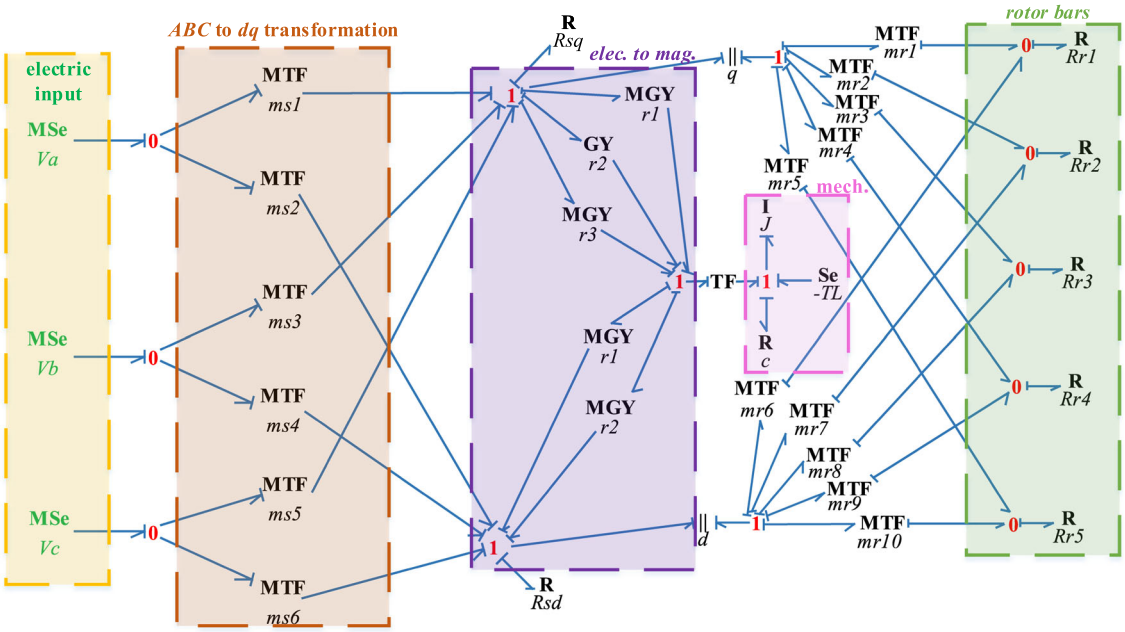

Fig. 5 The proposed bond-graph model with consideration of a hybrid rotor topology for a sample LSPMSM with 5 rotor bars. *Rr1* to *Rr5* are each rotor bar resistance. *Rsq* and *Rsd* are stator winding resistance

current with the *d*-*q* axes rotor current from the equivalent circuit can be written in the form of $i_r = m\boldsymbol{A}i_{rdq}$ as follows:

$$\begin{bmatrix} i_{r1} \\ i_{r2} \\ \vdots \\ i_{rk} \end{bmatrix} = m \begin{bmatrix} \cos(\theta) & \sin(\theta) \\ \cos\left(\theta + \frac{2\pi}{n}\right) & \sin\left(\theta + \frac{2\pi}{n}\right) \\ \vdots & \vdots \\ \cos\left(\theta + \frac{2(n-1)\pi}{n}\right) & \sin\left(\theta + \frac{2(n-1)\pi}{n}\right) \end{bmatrix} \begin{bmatrix} i'_{qr} \\ i'_{dr} \end{bmatrix} \tag{27}$$

Note that i'_{qr} and i'_{dr} are the outputs of the ordinary differential equation system of the LSPMSM. Equation (27) allows one to convert the *d*- and *q*- axis currents calculated from the machine differential equations to the rotor bar currents.

As shown in (27), $\boldsymbol{A}$ is an orthogonal matrix with the rank of 2 for any rotor bar angle (θ). It has been proven that for a $m \times n$ orthogonal matrix ($m > n$) it is possible to find $n \times m$ matrix ($\boldsymbol{B}$) where the product of them gives an identical matrix ($\boldsymbol{BA} = I_n$) [41]. I_n is an identity matrix with the order of n. Matrix $\boldsymbol{B}$ is the left-inverse of $\boldsymbol{A}$ which is transpose of $\boldsymbol{A}$. Authors in [41] demonstrate the modulation index (m) of the product of $\boldsymbol{A^T}$ and $\boldsymbol{A}$ must be proportional to $\sqrt{2/n}$ to obtain the identity matrix where

$$BA = A^T A = m^2 \sqrt{\frac{n}{2}} \begin{bmatrix} 1 & 0 \\ 0 & 1 \end{bmatrix} \tag{28}$$

According to (26), the current of each bar has a relationship with the *d*-*q* axes rotor current. Therefore, the rotor bars resistance effect can be separately modelled in the BG using the MTFs presented in (29) and (30).

$$mr_k = m\cos(\theta + \frac{2(k-1)\pi}{n}) \text{where} k = 1, \ldots, \text{n} \tag{29}$$

$$mr_{k+n} = m\sin(\theta + \frac{2(k-1)\pi}{n}) \text{where} k = 1, \ldots, \text{n} \tag{30}$$

So, for each rotor bar a modulated gyrator should be defined in the BG model. Figure 5 shows the extended version of the proposed BG model with consideration of the rotor bars (hybrid rotor) for a five-bar LSPMSM. The consideration of five rotor bars facilitates a better understanding of BG model as it prevents repeating equations.

4 Simulation results and model validation

A 4-pole, 0.5-Hp, 1500-rpm LSPMSM is investigated for validation of the proposed BG model against FEA. It is important to highlight that the proposed BG model is not replacement for FEA, but FEA is used for verification as the most accurate simulation technique for electrical machines. A cross-section of the case study and its geometry information are presented in Fig. 6 and Table 2, respectively. The stator resistance is calculated using the sizing equation considering the end winding effect by (31) [45]. In (31), the number of turns per phase and parallel paths are shown by N_{turns} and a. The average length of the winding including

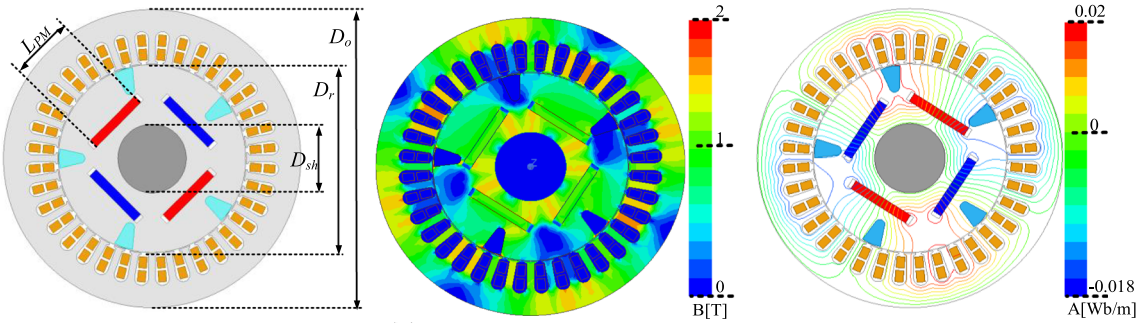

(a) The geometry and dimension of the considered LSPMSM. **(b)** 2D FEA results if the flux density distribution at no-load. **(c)** 2D FEA results if the flux lines at no-load.

Fig. 6 The cross section of the considered 4 poles, 5 bars, 0.5 HP LSPMSMs as the case study and its 2D FEA results of the no-load flux density and flux distribution

Table 2 Geometry dimensions of the studied LSPMSM as the case study for validation of the proposed BG model against FE analysis

Geometries and dimensions	Value	
L_{stack} [mm]	Stack length	100
D_{sh} [mm]	Shaft diameter	38
D_r [mm]	Rotor diameter	104
D_o [mm]	Stator outer diameter	136
L_{PM} [mm]	PM length	35
Th_{PM} [mm]	PM thickness	5
Hs [mm]	Stator slot height	14.1
Ws [mm]	Stator slot width	7.7
Hr [mm]	Rotor slot height	13
Wr [mm]	Rotor slot width	10.5
N_{turns}	Number of turns per phase	128
n	Number of rotor bars	5

Table 3 Parameters of the studied LSPMSM

Parameters	Value	
f (Hz)	Frequency	50
V_{rms} (V)	Applied voltage	415
P	Number of poles	4
P_m [W]	Rated power	367.75
R_s (Ω)	Stator resistance	5.09
R_r (Ω)	Rotor resistance	1.85
R_{r1}, R_{r2}, R_{r3}, R_{r4}, R_{r5} (Ω)	Rotor bar resistance	9.25
L_{md} (H)	Magnetizing inductance of d-axis	0.05
L_{mq} (H)	Magnetizing inductance of q-axis	0.32
L_{ds}, L_{qs} (H)	Stator leakage inductance of d-q axis	0.014
L'_{dr}, L'_{qr}(H)	Rotor leakage inductance of d-q axis	0.014
J (kg.m^2)	Mechanical inertia	0.001
c (N.s/m)	Mechanical resistance	0.00
λ_m(Wb)	Permanent magnet flux linkage	0.99

the end winding length is defined by l_{av} (Table 3).

$$R_{dc} = \frac{N_{turns} l_{av}}{a \sigma_{cu} S_a} \tag{31}$$

The AC resistance is equal to the product of calculated DC-resistance with the AC factor ($R_s = k_R R_{dc}$). The AC factor is obtained using (32).

$$k_R = \varphi_1(\beta) + [\frac{m_{sl}^2 - 1}{3} - ((\frac{m_{sl}}{2})sin\frac{\theta}{2})^2]\psi_1(\beta)$$

$$\beta = h_c \sqrt{\pi f \mu_0 \sigma_1 \frac{b_{con}}{B_{s2}} \frac{L_i}{L_b}}$$

$$\varphi_1(\beta) = \beta \frac{\sinh 2\beta + sin2\beta}{\cosh 2\beta - \cos 2\beta}$$

$$\psi_1(\beta) = 2\beta \frac{\sinh \beta - sin\beta}{\cosh \beta + \cos \beta} \tag{32}$$

m_{sl} : numberofconductorsperslotarrangedaboveeachother

b_{con} : widthofalltheconductorsinaslot

B_{s2} : $slotwidth$

l_e : lengthoftheendwidingwhichisassuemd0.6timesoftotalstatorlength

h_c : height of a conductor in the slot

L_b : Lengthofconductorbar

θ : phaseanglebetweentwolayers

The stator and rotor leakage inductances and the rotor resistances are obtained from the locked rotor test [46]. The end ring resistance ($\mathbf{R_{er}}$) is calculated using the sizing equations by (33) [47],

$$R_{er} = \left(\frac{2\pi r_{ring}}{N_b}\right) + \left(\frac{H_{er}}{2}\right)/\left(4A_{er}\sin^2(p\beta/N_b)\right), \quad (33)$$

where $\mathbf{r_{ring}}$, H_{er}, and A_{er} are the middle radius, height, and area of the end ring. The number of rotor bars and number of poles are shown by N_b and p, respectively. The obtained end ring resistance in the rotor side is 11.21 $\mu\Omega$. The obtained rotor resistance from the locked rotor test includes the portion of the end ring resistance transferred to the stator side. The magnetizing inductance is achieved using the open circuit and short circuit test results when the shaft rotates at rated speed using the torque equation introduced in [48]. PM flux linkage (λ_m) is determined using the open circuit test results [48].

The motor is modeled via Ansys® Electromagnetics [49] and the simulation results at no-load and full-load conditions are compared with the proposed BG model. The accuracy of the proposed BG model is validated with the FEA results.

4.1 The dynamic performance prediction in healthy rotor

In this section, the proposed BG model results of the case study are compared against FEA results for no-load and full-load dynamics. Figures 7 and 8 show the transient operation of torque, speed, and current of the case study at no-load and full load operation. Although the BG model cannot predict the first peak of the torque, it can properly follow the damping time and the waveform of the torque at healthy condition (see Figs. 7a and 8a). Although BG model cannot predict the initial speed undershoot of the LSPMSM when it starts from the stand-still, the average of the transient speed reposes in both bond graphs and FEA are the same (see Figs. 7b and 8b). The rotor speed is highly damped, and the final operating condition attend without any oscillation.

The rotor crawling (i.e., first speed notch) is predicted at the starting of the motor when it is run under 2Nm load. The current waveform is estimated with an acceptable accuracy from starting to steady state (see Figs. 7c and 8c).

4.2 The dynamic performance prediction under broken rotor bar condition

Demagnetization faults, stator winding faults, bearing faults, and broken rotor bars are common faults occurring in these types of electric machines. Modelling of the broken rotor bar fault and analysis of its effect on the performance parameters are more complicate than the other types of faults.

The demagnetizing of magnets, winding fault, and bearing faults affect the performance of the electric machine dramatically. As an example, if PMs are demagnetized, the motor will be unable to synchronize. The speed sensors can detect this phenomenon. The winding fault leads to the increment of the winding temperature. It can be detected by temperature monitoring.

When just a rotor bar is broken in the electric machine, the machine can continue to operate. In the presence of a faulty bar the loading and temperature on different bars are increased which results in a gradual damage to the rest of the bars. This type of fault is chosen to check the performance of the BG model. The bars of the cage can be broken due to the motor aging. The failure of the rotor bars affects the dynamics of the motor especially when it is energized from the stand-still [50–52]. Therefore, availability of a model capable of the determination of the rotor bar failures is useful when they are interconnected to different parts of a larger system.

The broken rotor bar test can be carried out using the proposed BG model. It is assumed that one of the rotor bars have been broken and the considered bar is operating as an open-circuit system. So, the resistance value for the considered broken bar is infinity in the BG model.

The simulation results demonstrate the capability of the BG model in predicting the effect of the broken rotor bar in the performance of the LSPMSM with respect to the 2D FEA results (see Figs. 9 and 10 for no-load and full-load results of the dynamics analysis, respectively). Figure 9 shows that the BG model can predict the steady state no-load torque, speed, and current at broken rotor bar condition. Figure 10 shows the BG model follows the LSPMSMs oscillation with a broken rotor bars when it starts operation at the rated load. The predicted torque ripple amplitude, speed fluctuations, and current fairly match with the 2D FEA results.

It should be highlighted that there are disparities between the BG and 2-D FEA results during the transient condition. The saturation of the iron parts during the transient is responsible for this disparity. The large starting current running through the stator winding and rotor bars results in local saturation. The saturation changes the machine inductances. Since BG model uses the constant inductances, the predicted performance during transient condition does not follow the 2-D FEA results.

The machine behavior is examined when two rotor bars are broken in the case study. Figure 11 shows the current waveform of the machine at no-load and full-load operations. According to the presented results, the calculated currents by BG model in both conditions are in a good agreement with the 2D FEA results. The difference between these models during the starting is resulted from the saturation of the d- and q- axes inductance which are ignored in the BG model. Due to the

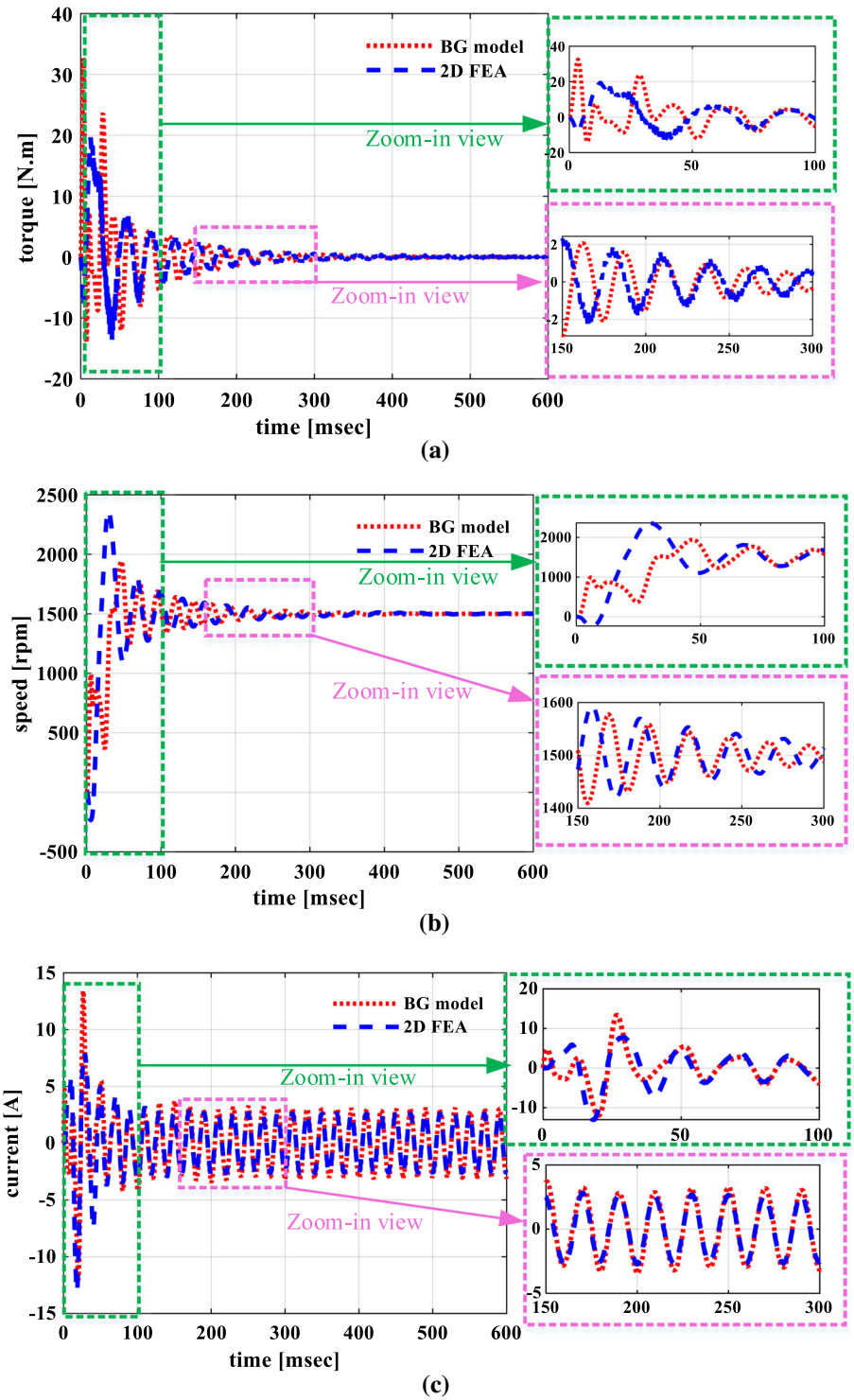

Fig. 7 Comparison of the proposed BG model with 2D FEA results in prediction of the dynamics of the LSPMSM at no-load condition. **a** torque versus time. **b** speed versus **c** current variation of phase A for different models (rms value of current at steady state is 2.12A)

limited numbers of rotor bars of the case study, the machine is not started promptly under 2Nm from standstill. So, a high current level flows through the windings (see Fig. 11b). The machine torque is presented in Fig. 12. It is seen that the BG model still predicts the performance with an acceptable accuracy.

4.3 Discussion on the Dynamics of LSPMSM

The comparison of the dynamic response of the LSPMSM during starting from the stand-still at no-load condition (Fig. 7) with the healthy rotor bars and broken rotor bars (Fig. 9) shows that:

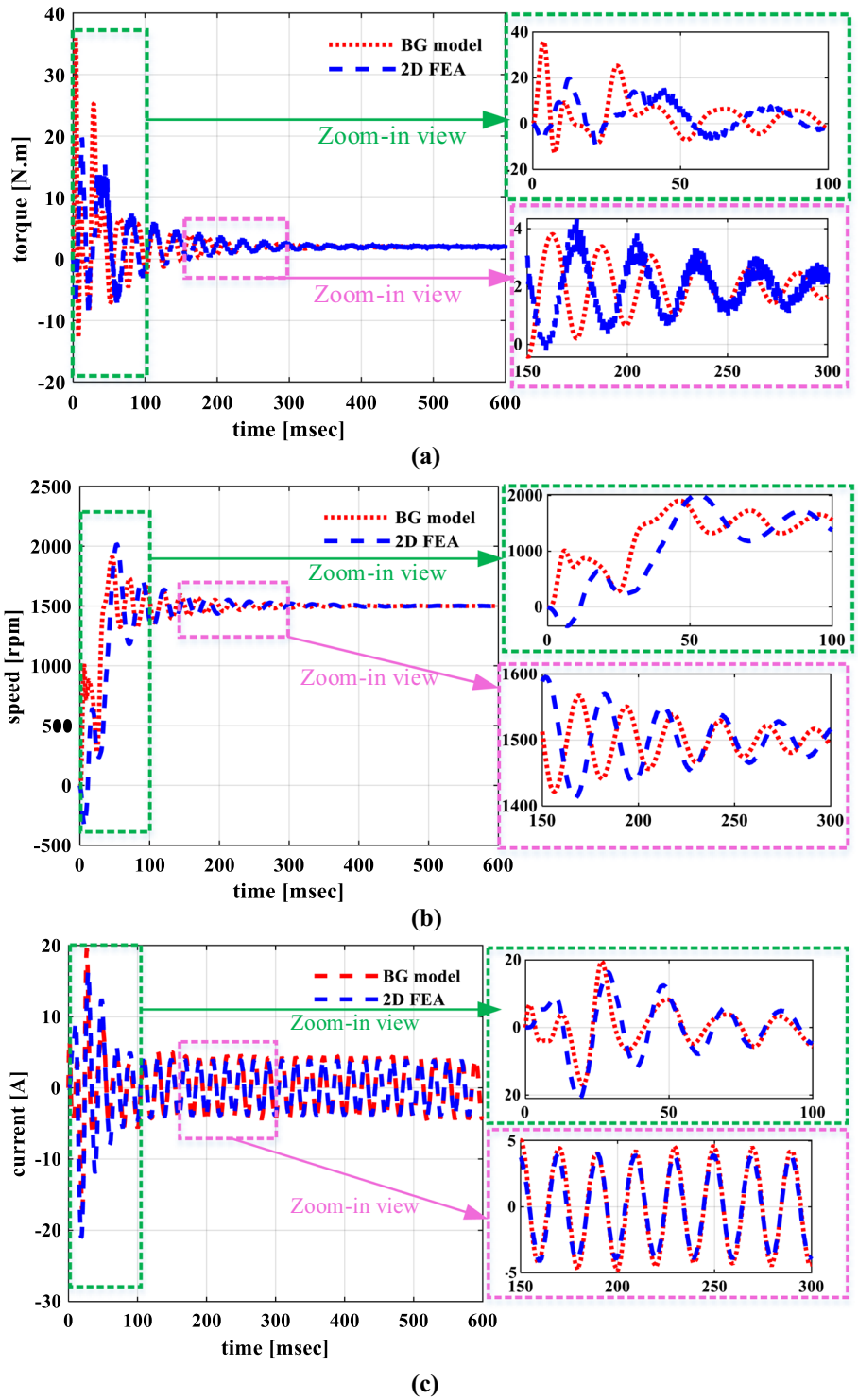

Fig. 8 Comparison of the proposed BG model with the 2-D FEA results at full-load condition for healthy LSPMSM. **a** torque versus time. **b** speed versus time. **c** current variation of phase A (rms value of current at steady state is 3.54A)

- The starting torque at the broken rotor (i.e., 53.6 Nm) is higher than the starting torque of the LSPMSM with a healthy cage (i.e., 50Nm).
- There is a speed notch in the dynamics of the broken rotor bar resulted from the effect of the asymmetrical flux distribution in the rotor. Also, an irregular speed oscillation is observed in the rotor bar broken condition at the starting.

The increment of the starting torque results from the increment of the rotor resistances. The notch in the speed response shows the rotor crawling at the starting. The crawling not only is resulted from the flux distribution asymmetry but also the asymmetrical induced current at the rotor bars located around the rotor leads to the crawling. The crawling effect in a motor

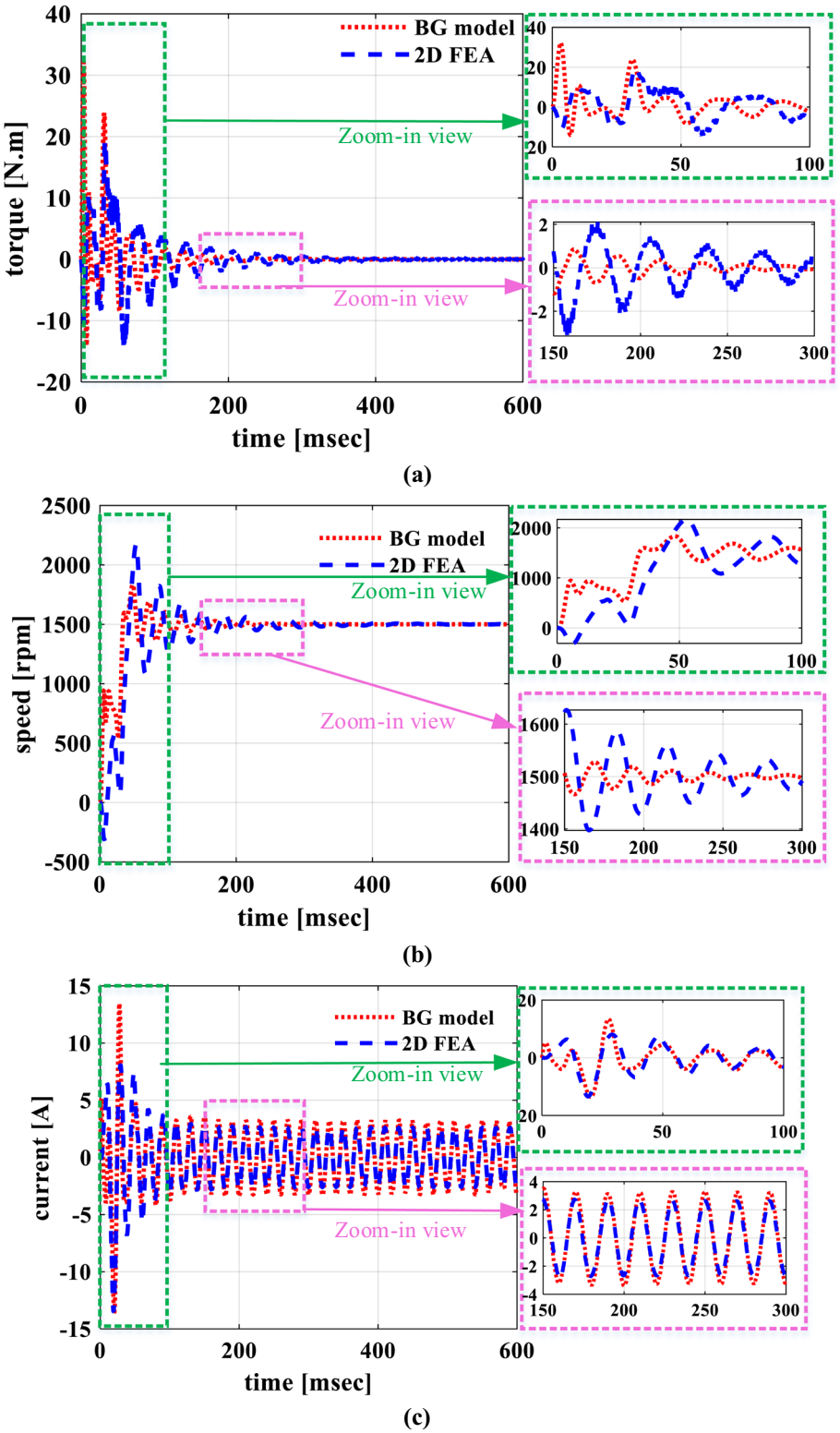

Fig. 9 Comparison of the predicted dynamics of the case study form the proposed BG model with the 2-D FEA results at no-load in the presence of a faulty open-circuited rotor bar. **a** torque versus time. **b** speed versus time. **c** current variation of phase A

with higher number of bars can be smaller when just one or two bars are broken.

Comparison of the Figs. 8 and 9 demonstrates that the dynamics of the starting of the case study under 2Nm load in the healthy and faulty cage is different in terms of the oscillations before reaching the steady-state and settling time. The torque reaches the steady-state operation in the healthy cage faster than the faulty cage. Also, the torque ripple of the faulty

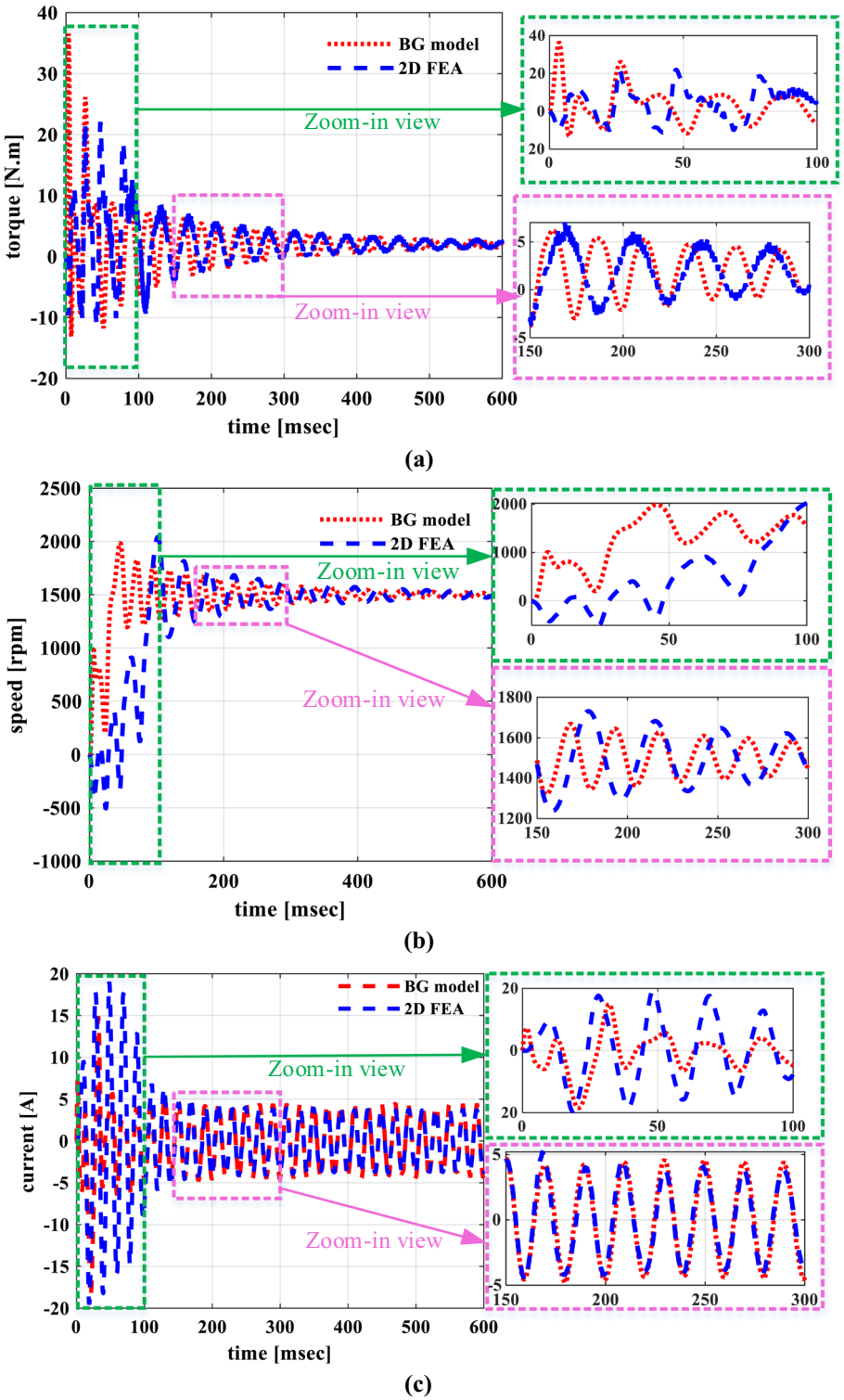

Fig. 10 Comparison of the proposed BG model with the conventional 2-D FEA in prediction of the dynamic performance of the LSPMSM at full-load operation in the presence of a broken rotor bar. **a** torque versus time. **b** speed versus time. **c** current variation of phase A

cage during the steady-state condition is 10% which is higher than the healthy rotor with the torque ripple of 8%. The rotor crawling time in the broken bar condition is approximately two times of the crawling time at the healthy cage (compare Fig. 8(b) and Fig. 10(b)).

The extracted results in Figs. 7, 8, 9 and 10 confirm that the stator current waveform is predicted with higher accuracy during the transient period as compared to the torque and speed curves. It is mainly due to the variation of the saturation level during transient condition which affects the *d*- and *q*-axis inductances. The inductance changes lead to the flux

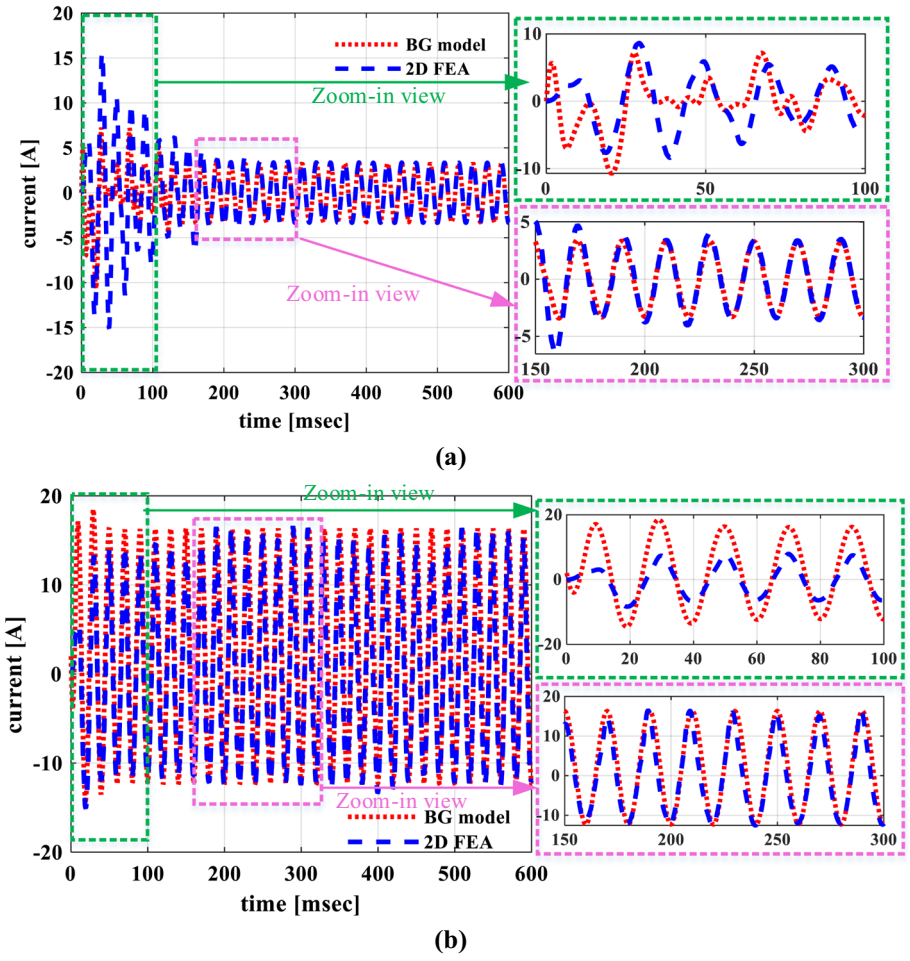

Fig. 11 Currents waveform of the case study when two rotor bars are broken. **a** at no-load. **b** under 2 Nm loading

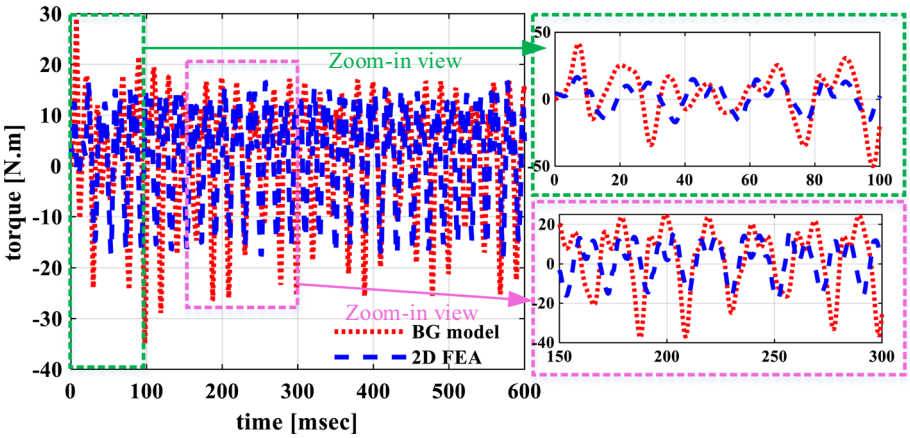

Fig. 12 Comparison of the BG model and 2D FEA results when the case study is excited from stall condition under 2 Nm load

change where plays a determinative role in torque and speed calculation (see Eqns. (10) and (13)).

5 Conclusion

The bond-graph model of a line-start permanent-magnet synchronous motor (LSPMSM) was introduced in this paper. The introduced bond-graph covered the magnetic, electrical, and mechanical energy domains of the LSPMSMs. The proposed BG was used to predict dynamics of a LSPMSM. The calculated dynamics was validated using the finite-element analysis results under two operating conditions: (1) a healthy motor, and (2) a motor with broken rotor bars. The simulation results demonstrated the accuracy of the proposed model in performance prediction of the LSPMSM in both transient and steady-state operations. The BG model predicts the performance parameters of the machine within 3 s which is 400

times less than the required time for FEA. Considering the accuracy and fast calculation speed, the proposed BG model of LSPMSM can be used in BG modelling of complex systems in which the LSPMSM is an integrated part.

Future work could include the application of BG modelling of LSPMSMs in analysis of static and dynamic air-gap irregularities, rotor eccentricity, demagnetization, and condition monitoring in is the existence of a control system for an integrated electromechanical system. The consideration of the saturation phenomenon can be another subject of the study in future. It can improve the accuracy of the model for prediction of the performance parameters especially during the transient behavior condition.

Funding Open Access funding enabled and organized by CAUL and its Member Institutions.

Declarations

Conflict of interest The authors declare that they have no conflict of interest.

References

1. Conti J, Holtberg P, Diefenderfer J, LaRose A, Turnure JT, and Westfall L, (2016) International energy outlook 2016 with projections to 2040. USDOE Energy Information Administration (EIA), Washington, DC
2. Krarti M (2020) Energy audit of building systems: an engineering approach. CRC Press, London
3. Roshandel E, Mahmoudi A, Kahourzade S, and Soong W, (2020) Analytical model and performance prediction of induction motors using subdomain technique. In: ECCE 2020 - IEEE energy conversion congress and exposition, pp. 3815–3822, doi: https://doi.org/10.1109/ECCE44975.2020.9235826.
4. Dianati B, Kahourzade S, Mahmoudi A (2020) Optimization of axial-flux induction motors for the application of electric vehicles considering driving cycles. IEEE Trans Energy Convers. https://doi.org/10.1109/TEC.2020.2976625
5. Angadi S, Yargatti UR, Suresh Y, Raju AB (2022) Speed sensorless maximum power point tracking technique for SEIG-based wind energy conversion system feeding induction motor pump. Electr Eng. https://doi.org/10.1007/s00202-022-01519-2
6. Sethupathi P, Senthilnathan N (2020) Comparative analysis of line-start permanent magnet synchronous motor and squirrel cage induction motor under customary power quality indices. Electr Eng 102(3):1339–1349
7. Banchhor DK, Dhabale A (2022) Novel formulation for optimized winding and core design for improved induction machine performance. Electr Eng 104(2):643–655
8. Šekara TB, Blanuša B, Knežević BZ (2018) A new analytical approach for design of current and speed controllers in electrical motor drives. Electr Eng 100(4):2789–2797
9. Aree P (2018) Precise analytical formula for starting time calculation of medium-and high-voltage induction motors under conventional starter methods. Electr Eng 100(2):1195–1203
10. Kahourzade S, Mahmoudi A, Ravji R, and Soong WL, (2019) Line-start axial-flux PM motors: introduction of a new machine topology. In: 2019 IEEE energy conversion congress and exposition (ECCE), pp. 7027–7034, doi: https://doi.org/10.1109/ECCE.2019.8912992
11. Barbara-Anne Kerslake SK, Mahmoudi A, (2021) Line-start permanent-magnet synchronous motor versus induction motor: technical, environmental and economical considerations. In: ECCE Asia 2021, pp. 1–8
12. Mahmoudi A, Rahim NA, Hew WP (2011) An analytical complementary FEA tool for optimizing of axial-flux permanent-magnet machines. Int J Appl Electromagn Mech 37(1):19–34
13. Jędryczka C, Knypiński Ł, Demenko A, Sykulski JK (2018) Methodology for cage shape optimization of a permanent magnet synchronous motor under line start conditions. IEEE Trans Magn 54(3):1–4
14. Bergman O, Nyborg L (2010) Evaluation of sintered properties of PM steels based on Cr and Cr-Mn prealloyed steel powders. Powder Metall Prog 10(1):1–19
15. McCallum RW, Kadin AM, Clemente GB, Keem JE (1987) High performance isotropic permanent magnet based on Nd-Fe-B. J Appl Phys 61(8):3577–3579
16. Roshandel E, Mahmoudi A, Kahourzade S, Yazdani A, Shafiullah GM (2021) Losses in efficiency maps of electric vehicles: an overview. Energies. https://doi.org/10.3390/en14227805
17. Tian M, Wang X, Wang D, Zhao W, Li C (2018) A novel line-start permanent magnet synchronous motor with 6/8 pole changing stator winding. IEEE Trans Energy Convers 33(3):1164–1174
18. Kahourzade S, Mahmoudi A, Roshandel E, Cao Z (2021) Optimal design of axial-flux induction motors based on an improved analytical model. Energy 237:121552. https://doi.org/10.1016/j.energy.2021.121552
19. Stockman K, Dereyne S, Vanhooydonck D, Symens W, Lemmens J, and Deprez W (2010) Iso efficiency contour measurement results for variable speed drives. In: The XIX international conference on electrical machines - ICEM 2010, pp. 1–6, doi: https://doi.org/10.1109/ICELMACH.2010.5608035.
20. Ferreira FJTE, Leprettre B, De Almeida AT (2016) Comparison of protection requirements in IE2-, IE3-, and IE4-class motors. IEEE Trans Ind Appl 52(4):3603–3610
21. Roshandel E, Mahmoudi A, Kahourzade S, Soong WL (2022) Saturation consideration in modeling of the induction machine using Subdomain technique to predict performance. IEEE Trans Ind Appl 58(1):261–272. https://doi.org/10.1109/TIA.2021.3125915
22. Mahmoudi A, Kahourzade S, Rahim NA, Ping HW, Ershad NF (2012) Slot-less torus solid-rotor-ringed line-start axial-flux permanent-magnet motor. Prog Electromagn Res 131:331–355
23. Saleeb H, Kassem R, Sayed K (2022) Artificial neural networks applied on induction motor drive for an electric vehicle propulsion system. Electr Eng 104(3):1769–1780
24. Ding H, Sixel W, Liu M, Li Y, and Sarlioglu B (2018) Influence of rotor pole thickness on optimal combination of stator slot and rotor pole numbers in integrated flux-switching motor-compressor.

In: 2018 IEEE energy conversion congress and exposition (ECCE), 2018, pp. 6893–6900
25. Adair D and Jaeger M, (2014) An integrated centrifugal pump rotor design course. In: Fourth interdisciplinary engineering design education conference, pp. 6–11
26. Almounajjed A, Sahoo AK, Kumar MK (2022) Condition monitoring and fault detection of induction motor based on wavelet denoising with ensemble learning. Electr Eng. https://doi.org/10.1007/s00202-022-01523-6
27. Thoma JU (2016) Introduction to bond graphs and their applications. Elsevier, London
28. Karimaghaee P, Hosseinzadeh A, Amidi A, and Roshandel E, (2017) Adaptive control application on syringe pump pressure control systems in oil and gas industries. In: 2017 5th international conference control instrumentation, and automation pp. 259–264, doi: https://doi.org/10.1109/ICCIAutom.2017.8258689
29. De León F, Purushothaman S (2013) Closed-form computation of electromagnetic fields in induction motors. Int J Power Energy Syst 33(2):62–70. https://doi.org/10.2316/Journal.203.2013.2.203-5079
30. Sen A, Majumder MC, Banerjee N (2018) Use of bond graph technique for rotor dynamic ssystem modelling and comprative analysis of vibration frequency using fast fourier transform. Int J Mech Prod Eng Res Dev 8(2):1151–1160
31. Isfahani AH, Vaez-Zadeh S (2009) Line start permanent magnet synchronous motors: challenges and opportunities. Energy 34(11):1755–1763
32. Kahourzade S, Mahmoudi A, Hew WP, and Uddin MN, (2013) Design and performance improvement of a line-start PMSM. In: 2013 IEEE energy conversion congress and exposition, pp. 5042–5047
33. Montazeri-Gh M, Fashandi SAM (2017) Application of Bond Graph approach in dynamic modelling of industrial gas turbine. Mech Ind 18(4):410
34. Munari E, Morini M, Pinelli M, Spina PR (2017) Experimental investigation and modeling of surge in a multistage compressor. Energy Procedia 105:1751–1756
35. Bhave SR and Kulkarni SA, Bond graph modeling of single stage reciprocating air compressor
36. Göing J, Kellersmann A, Bode C, and Friedrichs J, (2019) Jet propulsion engine modelling using pseudo bond graph approach. In: Turbo expo: power for land, sea, and air, vol. 58547, p. V001T01A007
37. Gawthrop PJ, Bevan GP (2007) Bond-graph modeling. IEEE Control Syst Mag 27(2):24–45
38. Broenink JF (1999) Introduction to physical systems modelling with bond graphs. SiE Whiteb Simul Methodol 31:2
39. Gawthrop PJ, Bevan GP (2007) A tutorial introduction for control engineers. IEEE Control Syst 27(2):24–45. https://doi.org/10.1109/MCS.2007.338279
40. Ghosh BC, Bhadra SN (1993) Bond graph simulation of a current source inverter driven induction motor (csi–im) system. Electr Mach power Syst 21(1):51–67
41. Kim J, Bryant MD (2000) Bond graph model of a squirrel cage induction motor with direct physical correspondence. J Dyn Sys Meas Control 122(3):461–469
42. Teng L, Yanjie L, and Lining S, (2010) Bond graph model of permanent magnet linear synchronous motor. In: 2010 2nd international conference on industrial and information systems, vol. 2, pp. 128–131
43. Rabbi SF, Rahman MA (2013) Critical criteria for successful synchronization of line-start IPM motors. IEEE J Emerg Sel Top Power Electron 2(2):348–358
44. Hancock NN (2016) Matrix analysis of electrical machinery. Elsevier, London
45. Gieras JF (2002) Permanent magnet motor technology: design and applications. CRC Press, London
46. Maraaba LS, Al-Hamouz ZM, Milhem AS, Twaha S (2019) Comprehensive parameters identification and dynamic model validation of interior-mount line-start permanent magnet synchronous motors. Machines 7(1):4
47. Boldea I (2020) Induction machines handbook. CRC Press, London
48. Odhano SA et al (2016) Identification of three-phase IPM machine parameters using torque tests. IEEE Trans Ind Appl 53(3):1883–1891
49. "Ansys® Electromagnetics." 2021, [Online]. Available: https://www.ansys.com/academic/terms-and-conditions
50. Saghafinia A, Kahourzade S, Mahmoudi A, Hew WP, and Uddin MN, (2012) On line trained fuzzy logic and adaptive continuous wavelet transform based high precision fault detection of IM with broken rotor bars. In: 2012 IEEE industry applications society annual meeting, pp. 1–8
51. de la Barrera PM, Otero M, Schallschmidt T, Bossio G, Leidhold R (2020) Active broken rotor bars diagnosis in induction motor drives. IEEE Trans Ind Electron 68:7556–7566
52. Dias CG, Pereira FH (2018) Broken rotor bars detection in induction motors running at very low slip using a Hall effect sensor. IEEE Sens J 18(11):4602–4613